Regulation of Multistep Spin Crossover Across Multiple Stimuli in a 2-D Framework Material

Manan Ahmed, Katrina Zenere, Natasha Sciortino, Kasun Arachchige, Gemma Turner, Jace Cruddas, Carol Hua, Jason Price, Jack Clegg, Francisco Valverde-Muñoz, et al.

The regulation of multistep spin-crossover across multiple stimuli in a 2-D framework material

Manan Ahmed,[1] Katrina A. Zenere,[2] Natasha F. Sciortino,[2] Kasun S. A. Arachchige,[3] Gemma F. Turner,[4] Jace Cruddas,[5] Carol Hua,[6] Jason R. Price,[7] Jack K. Clegg,[3] Francisco Javier Valverde-Muñoz,[8] Jose A. Real,[8] Guillaume Chastanet,[9] Stephen A. Moggach,[4] Cameron J. Kepert,[2]* Benjamin J. Powell,[5]* Suzanne M. Neville[1]*

[1]*The School of Chemistry, UNSW Sydney, Sydney 2052, New South Wales, Australia;* [2]*The School of Chemistry, The University of Sydney, Sydney 2006, New South Wales, Australia;* [3]*School of Chemistry and Molecular Biosciences, The University of Queensland, St Lucia 4072, Queensland, Australia*; [4]*School of Molecular Sciences, The University of Western Australia, Perth, Western Australia 6009, Australia;* [5]*School of Mathematics and Physics, The University of Queensland, St Lucia, Queensland 4072, Australia;* [6]*School of Chemistry, The University of Melbourne, Parkville, Victoria 3010, Australia;* [7]*The Australian Synchrotron, 800 Blackburn Road, Clayton, Victoria, Australia; Insitut de Ciencia Molecular, Department de Quimica Inorganica, Universitat de Valéncia, Patterna, Valéncia 46980, Spain ;* [9]*Univ. Bordeaux, CNRS, Bordeaux-INP, ICMCB, UMR 5026, F-33600, Pessac, France*

ABSTRACT: We investigate the effects of a broad array of external stimuli on the structural, spin-crossover (SCO) properties and nature of the elastic interaction within the 2-D Hofmann framework material $[Fe(cintrz)_2Pd(CN)_4]$·guest (cintrz = N-cinnamalidene 4-amino-1,2,4-triazole; **A**·guest; guest = $3H_2O$, $2H_2O$ & Ø). This framework exhibits a delicate balance between ferro- and antiferro-elastic interaction characters; we show that manipulation of the pore contents across guest = $3H_2O$, $2H_2O$ and Ø can be exploited to regulate this balance. In **A**·$3H_2O$, dominant antiferroelastic interaction character between neighboring Fe^{II} sites sees the low temperature persistence of the mixed spin-state species {HS-LS}, for {Fe1-Fe2} (HS = high spin, LS = low spin). Elastic interaction strain is responsible for stabilizing the {HS-LS} state and can be overcome by three mechanisms: (1) partial ($2H_2O$) or complete (Ø) guest removal, (2) irradiation via the reverse-LIESST effect (λ = 830 nm; light-induced excited spin-state trapping) and (3) the application of external hydrostatic pressure. Combining experimental data with elastic models presents a clear interpretation that while guest molecules cause a negative chemical pressure, they also have consequences for the elastic interactions between metals beyond the simple chemical pressure picture typically proposed.

INTRODUCTION

The development of externally addressable molecule-based materials with precisely and predictably controlled physical properties is an integral step to the advancement of molecular device components.[1] Cultivating a holistic understanding of the structure and properties of such materials at a fundamental level and across multiple stimuli is a key-step towards achieving tunability and widespread applicability of these functional materials. To this end, spin-crossover (SCO) materials are a clear target as spin-state switching is accessible via a range of established mechanisms, including temperature, light-irradiation, and the application of pressure.[2-3]

Irrespective of the applied SCO perturbation method, an intrinsic link between structure and function exists.[4] This is since the SCO phenomenon depends intimately on the nature of elastic interactions in the solid-state.[5] Consequently, detailed crystallographic studies are a critical tool for providing a precise understanding at the atomic level.[6] Of similar importance is to combine such studies with theoretical models so that comprehensive interpretations can be constructed. Illustrating the extreme utility of this approach, experimental and theoretical studies have collectively provided a chemical toolbox to reliably achieve multi-stepped SCO. These studies have shown that inserting structural features that cooperate or compete depending on the network of ferroelastic and antiferroelastic interactions drives multistep SCO.[7] Both theory and experiment have shown that this can be achieved by synthetic components such as ligands and/or guest molecules with supramolecular interaction capacity.[7-8] This approach has been further applied to tune the balance between ferro- and antiferroelastic interaction character, through for example guest exchange or ligand functionalization, to produce programmable multistep SCO character.[8]

With all of this in mind, we utilize the well-developed structural and mechanistic picture of thermally-induced and guest-modulated multistep SCO, and extend this to include the perturbation methods of photoirradiation and hydrostatic pressure. To achieve this, we focus on 2-D Hofmann-type framework materials with functionalized 1,2,4-triazole ligands, which have been particularly successful at reliably producing thermally-active multistep SCO (with guest-tuneable features).[8a,9] So that a complete picture is established towards predictable and reliable switching across this broad spectrum of perturbation methods, we use a comprehensive array of experimental and theoretical methodologies.

RESULTS

Synthesis and characterization. Yellow square-shaped single crystals of $[Fe(cintrz)_2Pd(CN)_4]\cdot 3H_2O$ (**A**·$3H_2O$) were obtained by slow diffusion of $Fe(ClO_4)_2\cdot 6H_2O$, cintrz[10] and $K_2[Pd(CN)_4]\cdot H_2O$ in ethanol:water over 4 weeks. With exposure to air for 24 h partial desolvation occurs to form **A**·$2H_2O$. Heating pristine **A**·$3H_2O$ to 100 °C for 24 h removes all of the water to form **A**·Ø. The identity and purity of solvates were confirmed by thermogravimetric analysis (Figures S1-2), infrared spectroscopy, DSC (Figures S3-4), powder X-ray diffraction analyses (Figures S5-6) and single crystal X-ray diffraction (Figures S9-10).

Thermo-, photo-, and piezo-magnetic data. Plots of $\chi_M T$ versus temperature for **A**·$3H_2O$, **A**·$2H_2O$ and **A**·Ø are shown in Figure 1(a). On cooling **A**·$3H_2O$ the Fe^{II} sites maintain a HS character ($\chi_M T$ = ~3.46 cm^3 K mol^{-1}) above ~175 K, below which a rapid decrease in $\chi_M T$ values to ~1.50 cm^3 K mol^{-1} occurs; this is consistent with a 1:1 ratio of HS:LS sites that remains down to 10 K. Thermal hysteresis (ΔT = 15 K) is evident over the thermal cycle ($T_{½}\downarrow\uparrow$ = 171, 186 K for 2 $Kmin^{-1}$; see Figure S17 for other scan-rates). For **A**·$2H_2O$, a HS Fe^{II} character exists

above ~185 K, and below this a stepwise decrease in $\chi_M T$ values occurs to a fully LS Fe^{II} character below ~75 K ($\chi_M T$ = ~0.12 cm^3 K mol^{-1}). The 1:1 HS:LS state exists over a ~100 K temperature range. The characteristic transition temperatures of **A**·2H_2O are $T_{½}\downarrow\uparrow$ = 190, 203 K (ΔT = 13 K) and $T_{½}\downarrow\uparrow$= 93, 105 K (ΔT = 17 K) for a scan-rate of 2 $Kmin^{-1}$. There is some scan-rate dependence in the low temperature step (Figure S18) which reflects slow kinetics of this low transition temperature. For **A**·Ø, an abrupt one-step spin transition occurs (HS ↔ LS states), with negligible hysteresis ($T_{½}\downarrow\uparrow$: 145, 149 K; ΔT = 4 K).

After cooling a sample of **A**·3H_2O to 10 K, the LIESST effect[11] was examined by irradiation with green light (λ = 510 nm; Figure 1(b)). During this time, the $\chi_M T$ values increased to ~1.60 cm^3 K mol^{-1}. Then, in the absence of irradiation the temperature was increased to 100 K,[12] resulting in a $\chi_M T$ maximum at 30 K (*ca.* 2.15 cm^3 K mol^{-1}), followed by a rapid decrease back to the thermally stable HS:LS plateau. The characteristic LIESST temperature[13] for **A**·3H_2O is 38 K (Figure S19), as defined by $\delta\chi_M T/\delta T$ of the LIESST relaxation (*i.e.*, 10 – 100 K). The maximum $\chi_M T$ values achieved under green light irradiation indicate an incomplete (*ca.* 40%) conversion from the HS:LS state to the HS state.

After again cooling a sample of **A**·3H_2O to 10 K, the sample was irradiated with red light (λ = 830 nm) to investigate the reverse-LIESST effect (Figure 1(b)).[11] Over 1 h the $\chi_M T$ values decreased to ~0.01 cm^3 K mol^{-1}, consistent with a complete LS state and a 100% photo-conversion. Then, in the absence of irradiation the temperature was increased to 100 K,[12] resulting in an increase in $\chi_M T$ values back to the HS:LS plateau. The characteristic reverse-LIESST value is 96 K (Figure S20), as defined by $\delta\chi_M T/\delta T$ of the reverse-LIESST relaxation (*i.e.*, 10 – 100 K).[13] Direct, and repeatable switching between the LS and metastable HS states can be achieved by repeated irradiation using 510 nm then 830 nm irradiation (Figure S21). Monitoring the reverse-LIESST effect under constant irradiation (*i.e.*, one thermal cycle over the range 10 – 120 – 10 K under constant irradiation) showed a light-induced thermal hysteresis (LITH) loop with a 65 K width ($T_{½}\downarrow\uparrow$ = 90, 25 K).

A sample of **A**·3H_2O was loaded into a custom hydrostatic pressure cell and variable pressure measurements taken over the range 0 to 0.3 GPa (Figure 1(c)). At 10^5 Pa, the SCO properties are the same as ambient pressure ($T_{½}\downarrow\uparrow$: 177, 191 K; ΔT = 14 K). Increasing the pressure to 0.05 GPa triggers an increase in transition temperature ($T_{½}\downarrow\uparrow$: 215, 250 K; ΔT = 35 K) and a subtle, and asymmetric, two-step SCO character. At 0.08 GPa, the two-step SCO character is more apparent, with the higher temperature step indicative of a complete HS to HS:LS transition and the lower temperature step being an incomplete (*ca.* 25% HS:LS to LS) conversion ($T_{½}\downarrow\uparrow$ = 270, 278 K; ΔT = 8 K, and $T_{½}\downarrow\uparrow$= 100, 103 K; ΔT = 3 K). At 0.19 GPa, the two-step SCO character persists but is again increased to higher temperature. Here, the high temperature SCO loop at 0.19 GPa is shifted such that it occurs above room temperature. The low temperature loop shows a near complete HS:LS to LS transition. Finally, by 0.3 GPa, the transition temperature of the two-step character is shifted so that only the HS:LS to LS step is visible ($T_{½}\downarrow\uparrow$: 212, 218 K; ΔT = 6 K). With pressure release the ambient SCO properties are re-established.

We note that the pressure most likely changes subtly upon variation in temperature. This might increase the gradual character of the SCO or lead to some of the irregularities in the curves.

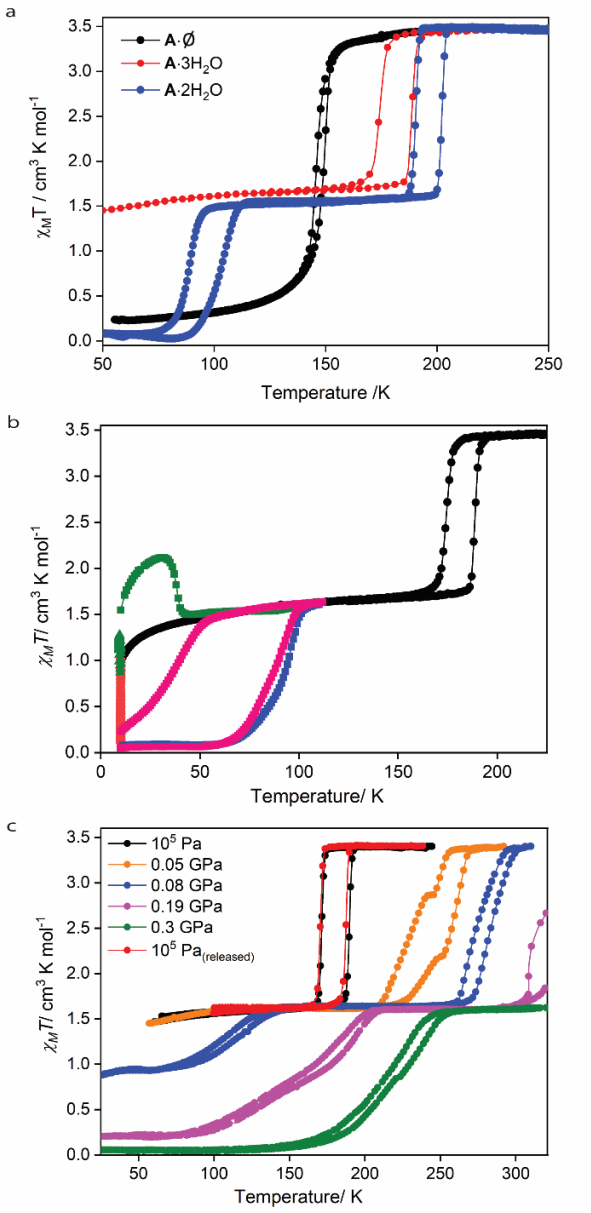

Figure 1. (a) χ_MT versus temperature for **A**·3H_2O, **A**·2H_2O and **A**·Ø (scan rate of 2 K min^{-1}). (b) **A**·3H_2O showing the thermal transition (black), LIESST effect (λ = 510 nm, ■) at 10 K followed by relaxation in the absence of light (10 – 100 K, ⍰), reverse-LIESST (λ = 830 nm, ⍰) at 10 K followed by heating in the absence of light (⍰) and LITH (λ = 830 nm, ⍰) effect. (c) **A**·3H_2O under variable pressure (10^5 Pa, 0.05, 0.08, 0.19, 0.3 GPa) contained in a hydrostatic pressure cell with silicon oil as the pressure transmitting medium.

Structural analyses across multiple stimuli. The structures of **A**·3H_2O & **A**·2H_2O were investigated by variable temperature powder X-ray diffraction and single crystal X-ray diffraction analyses to assess the impact of guest-loading and temperature variation on the structure. Powder X-ray diffraction data were collected using synchrotron radiation over the SCO temperature range (Figures S7-8). The temperature-dependence of the Bragg peaks show abrupt shifts coincident with the transition temperatures obtained from magnetic susceptibility for both **A**·3H_2O & **A**·2H_2O, thereby confirming the SCO behavior of the bulk sample (*cf.* magnetic susceptibil-

ity data). Single crystal X-ray diffraction data were collected for **A**·3H$_2$O over the range 200 – 165 – 200 K at 5 K intervals and for **A**·2H$_2$O over the range 250 – 95 – 250 K at 10 K intervals. Plots of the unit cell volume evolution versus temperature for each material closely match the SCO behavior determined by magnetic susceptibility (Figures S11-12). Close inspection of the powder diffraction and single crystal data reveals a retention of primitive triclinic ($P\bar{1}$) symmetry with temperature variation, without any evidence of a crystallographic phase transition, such as doubling of unit cell axes.

Structural solutions for **A**·3H$_2$O & **A**·2H$_2$O show asymmetric units comprised of two distinct Fe^{II} sites (Fe1 & Fe2), one [Pd(CN)$_4$]$^{2-}$ anion and two monodentate cintrz ligands (L_1 & L_2), an example of which is shown for **A**·3H$_2$O in Figure 2(a). Within the extended structure, each Fe^{II} centre is six-coordinate (FeN$_6$) with two axial cintrz ligands and four [Pd(CN)$_4$]$^{2-}$ anions. The Fe^{II} sites are situated at the nodes of 2-D layers with wine-rack topology (Figure 2(b)). The cintrz ligands (L_1 & L_2) protrude above and below the layers as illustrated in Figure 2(c)). The Fe1 and Fe2 sites are arranged in alternating stripes along the *a*-axis (Figure 2(b-c)). Neighboring layers are interdigitated via the head-to-tail alignment of cintrz ligands (Figure 2(d)) with aromatic contacts via the ligand alkyl chains (Table S2).

Layer undulation defines pairs of closely associated ligands which interact via host-host hydrogen-bonding interactions (Figure 2(c); Table S2). These are spaced along the *b*-axis by larger ligand voids which are occupied by guest molecules (Figure 2(c)). There are two distinct guest positions, the first being occupied in both **A**·3H$_2$O and **A**·2H$_2$O and containing one water molecule engaged in a hydrogen-bonding interaction with a triazole group (L_1…O), as depicted in Figure 2(c)). There is then an additional water molecule for **A**·3H$_2$O and a partially occupied water molecule for **A**·2H$_2$O (shown in Figure 2(c) as a shaded region); irrespective of the total occupancy, these molecules are disordered over two sites and engage in guest-guest interactions (Table S2).

The unit cell parameters of **A**·3H$_2$O and **A**·2H$_2$O in the HS state are closely similar, indicating that the structural effects of partial guest removal are minor and involve local changes. Potential changes to the Fe^{II} nodes were explored via assessment of the flexibility of different structural motifs in the framework, as summarized in Figure 3. Firstly, layer deformation was assessed by examining the relative layer undulation over the three symmetry unique tiles of the [Fe(Pd(CN)$_4$] layers (as defined in Figure 3(a-b)), revealing negligible difference between **A**·3H$_2$O and **A**·2H$_2$O (Table S2). Next, potential compression or expansion of the wine-rack topology (Figure 3(c)) was quantified by the grid 'hinge' angles (θ1: ∠N1-Fe1-N2 & θ2: ∠N7-Fe2-N8), also revealing minor change upon partial guest removal (Table S2). Similarly, little variation to the interlayer separation (Fe1…Fe2, Figure 3(d) is seen (Table S2). The most substantial variation occurs at the local Fe2 geometry, whereby the degree of octahedral distortion (Table S2)[14] at Fe2 is decreased in **A**·2H$_2$O (Σ^{Fe2}: 11.16 °) compared to **A**·3H$_2$O (Σ^{Fe2}: 14.4 °). The distortion at Fe1 is effectively unchanged (Σ^{Fe1}: 5.44, 5.84 °, for **A**·3H$_2$O and **A**·2H$_2$O respectively).

Detailed structural analyses for both **A**·3H$_2$O and **A**·2H$_2$O at the 1:1 plateau show that Fe1 remains in the HS state and Fe2 converts to the LS state, based on average Fe-N bond lengths (Table S2). The spin-state distribution of the [HS-LS] state, for [Fe1-Fe2], is alternating 1-D stripes of HS and LS states, as illustrated in Figure 2(b-c). For **A**·2H$_2$O, further cooling sees a complete LS state achieved based on Fe-N bond lengths (Table S2). Accompanying the spin-state transitions are variations to the octahedral distortions at Fe1 and Fe2. Notably, the degree of distortion at Fe1 increases substantially over the [HS-HS] ↔ [HS-LS] step (**A**·3H$_2$O (Σ^{Fe1}: 5.44 to 13.64 °, for 210 to 170 K) and **A**·2H$_2$O (Σ^{Fe1}: 5.84 to 14.4 °, for 250 to 150 K).[14] Hence, overall, the spin-state transition pathway across [Fe1-Fe2] for **A**·3H$_2$O is [HS-HS] ↔ [HS-LS] and for **A**·2H$_2$O is [HS-HS] ↔ [HS-LS] ↔ [LS-LS]. The other parameters shown in Figure 3 remain largely unchanged upon spin-state variation, except that greater LS fraction leads to reduced layer undulation in both **A**·3H$_2$O and **A**·2H$_2$O (Table S2).

Photo-induced single crystal X-ray diffraction analyses were conducted on **A**·3H$_2$O at 30 K under constant irradiation with red light to examine the reverse-LIESST structure. A crystal was cooled to 30 K, representative of the [HS-LS] state, and upon irradiation the unit cell parameters were seen to decrease over a period of 2 h (Table S3). The reverse-LIESST structure shows a decrease in average Fe-N bond length at both Fe1 and Fe2 (<d_{Fe-N}>: Fe1 = 2.00 Å and Fe2 = 1.96 Å), with Fe2 achieving complete LS state and Fe1 a partial conversion. We note that the experimental conditions were not identical to that of magnetic susceptibility (*i.e.*, 30 K *cf.* 10 K and LED light source *cf.* laser) resulting in incomplete conversion of the single crystal to the [LS-LS] state. Nevertheless, examination of the relative changes in local Fe^{II} site and framework flexibility show trends (Table S4) like those observed over the [HS-LS] to [LS-LS] transition for **A**·2H$_2$O, in particular, reduction of the relative octahedral distortion at Fe1 and Fe2, layer undulation and interlayer spacing. After irradiation, unit cell data were collected over the range 30 – 250 K revealing a two-step behavior passing through the intermediate [HS-LS] state (Figure S13), as per magnetic susceptibility.

High pressure single crystal X-ray diffraction analyses were conducted on **A**·3H$_2$O under hydrostatic pressure (0, 0.14, 0.36, 0.57, 1.01, 1.72, 2.75 GPa; Table S5). Visual inspection of a single crystal within a diamond anvil cell under hydrostatic compression showed a color change from pale yellow to red above 0.36 GPa (Figure S14). The unit cell volume evolution as a function of pressure at ambient temperature (Figure 4) shows a total volume compressibility over the 0 – 2.75 GPa range of 15.4%. There are three distinct regions of compressibility: (1) [HS-HS] state (0 – 0.36 GPa), (2) a SCO event (0.36 – 1.01 GPa) and (3) [LS-LS] state (1.01 – 2.75 GPa). The [HS-HS] region shows an overall compression of ΔV = 3%, which is consistent with normal pressure-induced compression of a solid of this type.[15] The bulk modulus for the HS and LS regions, respectively are 30 and 48 GPa, highlighting the difference in compressibility of the [HS-HS] and [LS-LS] states.[4,9e,f] The SCO region shows a compression of 6.8% (Figure S16), which is consistent with a pressure- induced SCO event.[4,9e,f] The linear compressibility over the entire 0 – 2.75 GPa range indicates that the *c*-axis (i.e., interlayer spacing) is the most responsive to pressure increase. This is in line with the presence of weak inter-layer interactions along this direction, compared to stronger intra-layer interactions in the *ab*-plane of the Hofmann layer. Detailed structural analyses at all pressures confirm a complete transition from the [HS-HS] to [LS-LS] states and suggests a transient stability of the [HS-LS] state at 0.57 GPa, based on average Fe-N bond lengths (Table S6). Examination of the changes to structure with pressure increase shows substantially greater distortion of both the local and extended structure (Figure S15). In particular, the octahedral distortion at both Fe1 and Fe2 are much greater

than that observed for **A**·2H_2O in the [LS-LS] state and **A**·3H_2O under red-light irradiation. Furthermore, the layer undulation and hinge angles are much greater, indicating increased layer distortion.

Figure 2. (a) Asymmetric unit of **A**·3H_2O (210 K) - disordered water molecules shown (O2A/B and O3A/B). (b) Structural representation of one Hofmann layer (001),

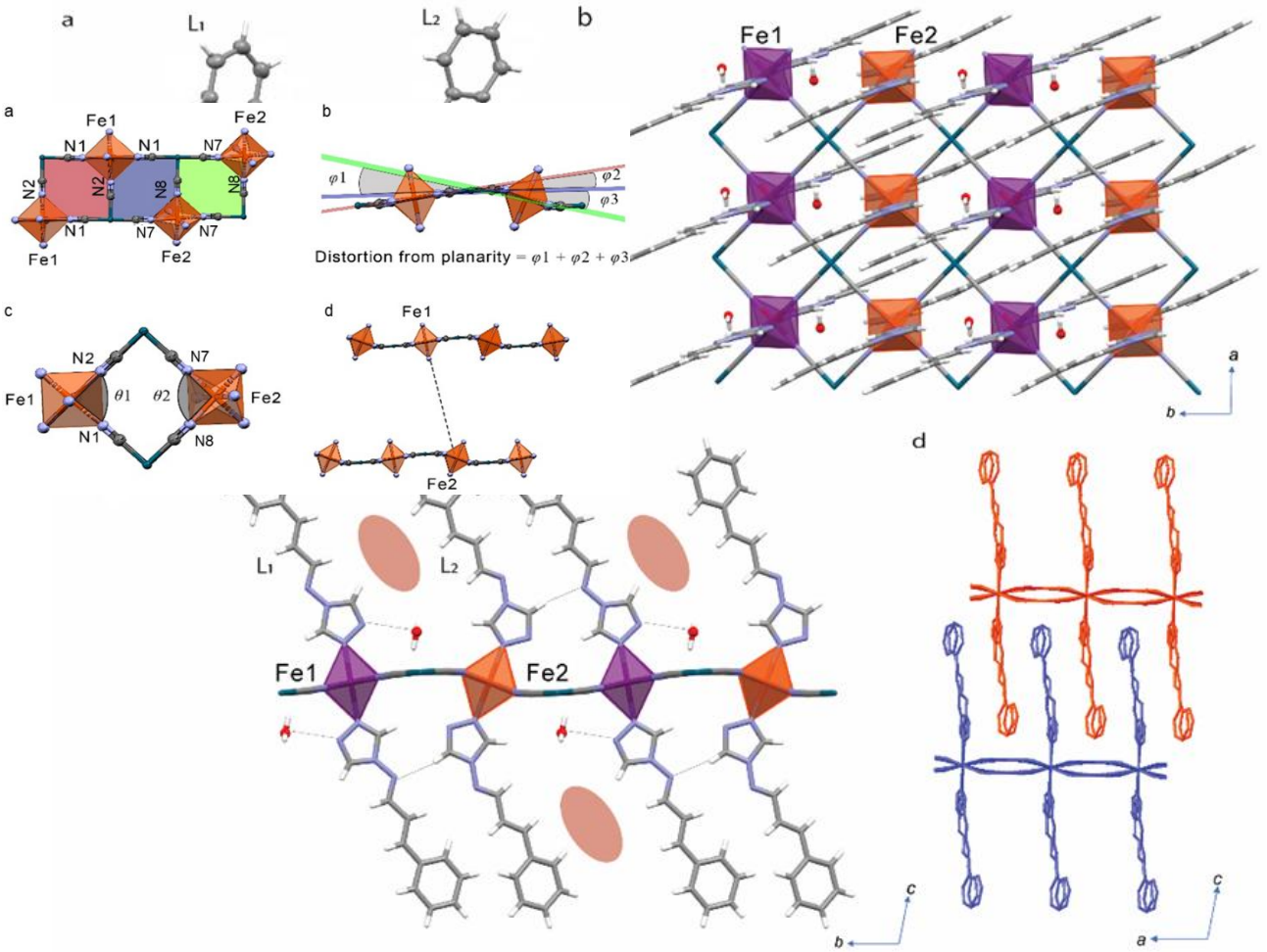

showing the cds, wine-rack topology with Fe1 and Fe2 in stripes connected by $[Pd(CN)_4]^{2-}$ units. (c) One Hofmann layer (100), highlighting the layer undulation, ligand (L_1 & L_2) position, host-host and host-guest interactions common to both **A**·3H_2O and **A**·2H_2O and labile pore region (shaded oval). Note: (b-c) show the distribution of LS Fe1 (purple) and HS Fe2 (orange) sites at the [HS-LS] state. (d) The head-to-tail interdigitation of ligands in neighboring layers (red and blue).

Figure 3. Definition of structural parameters. (a) three, symmetry unique tiles in the Hofmann layers, (b) the planes defined by the Fe and Pd ions in each square (as defined in (a)), the relative distortion from planarity is defined as $\varphi 1 + \varphi 2 + \varphi 3$, (c) the 'hinge' angles, $\theta 1$ = ∠N1-Fe1-N2 & $\theta 2$ = ∠N7-Fe2-N8 and (d) distance between Fe1 and Fe2 on adjacent layers.

Figure 4. Unit cell volume versus pressure (0 – 2.75 GPa) for **A**·3H_2O at ambient temperature. These data show three distinct regions of distinct compressibility correlating to the HS state (0 – 0.36 GPa), a SCO event (0.36 – 1.01 GPa) and the LS state (1.01 – 2.75 GPa).

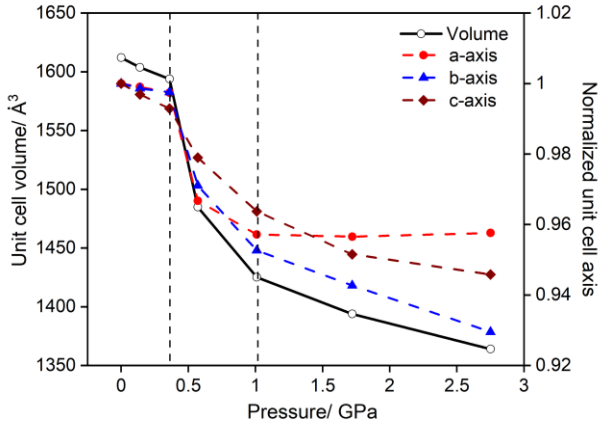

Elastic model. To better understand the implications of the above results, we considered an elastic model of balls with variable radii coupled by a network of springs. Specifically, we study the Hamiltonian

$$H = \sum_{n=0}^{5} H_n + pV, \qquad (1)$$

where p is the pressure, V is the total volume,

$$H_0 = \sum_i \frac{1}{2}(\Delta H - T\Delta S)\sigma_i = \frac{1}{2}\Delta G \sum_i \sigma_i,$$

$\Delta H = H^{HS} - H^{LS}$ is the single molecule enthalpy difference between the HS and LS states, $\Delta S = S^{HS} - S^{LS}$ is the single molecule entropy difference between the HS and LS states, $\Delta G = G^{HS} - G^{LS} = \Delta H - T\Delta S$ is the single molecule difference in the free energy,

$$H_n = \frac{k_n}{2} \sum_{\langle i,j \rangle_n} \left[r_{i,j} - \eta_n \left(\bar{R} + \delta(\sigma_i + \sigma_j) \right) \right]^2,$$

k_n is the elastic interaction between n^{th} nearest neighbours (see Fig. 6(a)), $r_{i,j}$ is the instantaneous lattice distance between sites i and j, $\eta_n \in \{1, \sqrt{2}, 2, \sqrt{5}, 2\sqrt{2}\}$ is a geometric factor that depends only on the topological relationship between i and j, $\bar{R} = (R^{HS} + R^{LS})/2$, $\delta = (R^{HS} - R^{LS})/4$, $R^{HS}(R^{LS})$ is the average distance between nearest neighbour iron atoms in the HS (respectively LS) phases and $\sigma_i = +1(-1)$ if the i^{th} molecule is in the HS (respectively LS) state.

We make the symmetric breathing mode approximation,[7b-c] i.e., we set $r_{i,j} = \eta_n x$ and assume the topology of the lattice is unaltered by changes in the spin-state, and minimize the resultant expression over x, resulting in an Ising-Husimi-Temperley model (details of the derivation can be found in the Supplementary Information). Note that the variable x still allows for uniform relaxation of the crystal structure as the temperature changes. We set $V = L^3 c x^2$, where L is the number of sites along one direction and c is the unit cell parameter; we chose this rather than, say, $V = L^3 x^3$ because c does not vary strongly or correlate straightforwardly with the SCO state, whereas the a- and b-unit cell parameters do (Figure S12).

For **A**·guest through-bond interactions connect the second and fifth nearest neighbour Fe^{II} ions (Figure 6(a)), thus we expect that $k_2 > k_5 \geq 0$, whereas the first, third and fourth nearest neighbour Fe^{II} ions are connected via through-space interactions (Figure 6(a)) including host-guest interactions, thus we expect that they will be negative[7c] with $k_1 < k_3 < k_4 \leq 0$. The relative contributions of the through-bond and through-space interactions have been shown to strongly affect the collective spin-state properties of SCO materials.[7c]

We report the phase diagram of the elastic model (Eq. 1) in Figure 5(a) (and Figure S22). For $k_1 \lesssim -0.78 k_2$ we observe an incomplete transition from [HS-HS] to [HS-LS] with stripe order (Figure 5(b)), similar to that observed in **A**·3H$_2$O (Figure 1(a)). For $-0.78 \lesssim k_1/k_2 \lesssim -0.32$ the transition occurs in two steps (Figure 5(c)) with intermediate stripe order (sketched in Figure 6(a)), consistent with our experimental findings for **A**·2H$_2$O (Figure 1(a)). While the overall two-step transition is consistent with experimental data, the low temperature hysteresis loop appears wider in the model. This difference is owing to the slow kinetics of this low temperature transition which was observed experimentally by variable scan-rate data (Figure S18) – scan-rate effects cannot be included in the model. For $k_1 \gtrsim -0.32\ k_2$ the transition becomes a one-step HS to LS transition with no intermediate ordering (Figure 5(d)), as we observe in **A**·∅ (Figure 1(a)). The curves shown in Figure 5(b)-(d) are the calculations for parameters that yield the best agreement with the measured $\chi_M T$ versus T curves.

We also report the pressure-temperature phase diagram for the elastic model (Eq. 1) in Figure 6(b-c). For pressure, $P \lesssim 0.025$ GPa we observe an incomplete transition from HS to stripe order (Figure 6(b-c) and for $P \gtrsim 0.025$ GPa the transition becomes complete with two-steps and intermediate stripe order (Figure 6(b-c)), both are consistent with our experimental findings (*cf.* Figure 1(c)).

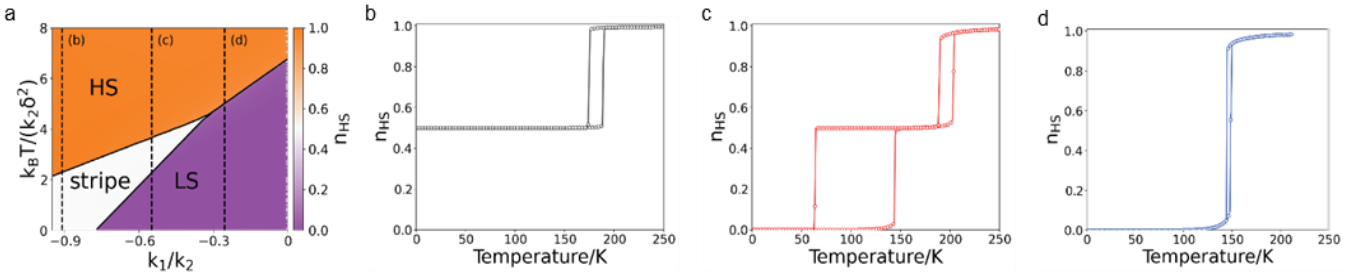

Figure 5. (a) Phase diagram of the elastic model (Eq. 1) on varying temperature and k_1, the (through space) nearest neighbor interaction with $k_3 = k_1/2$ and $\Delta H/k_2\delta^2 = 44\ k_1/k_2 + 43$ and fixed k_2 the (through bond) second nearest neighbour interaction and δ half the difference in distance between neighbouring Fe^{II} metal ions. (b-d) Calculated fractions of HS metals for parameters that reproduce the experimentally measured $\chi_M T$ curves: in all three plots $\Delta S = 4\ k_B \log(5)$ with (b) $k_1\delta^2 = -72.8$ K, $k_2\delta^2 = 80$ K, $\Delta H = 3.0$ K; (c) $k_1\delta^2 = -30.25$, $k_2\delta^2 = 55$ K, $\Delta H = 18.8$ K; and (d) $k_1\delta^2 = -7.8$ K, $k_2\delta^2 = 30$ K, $\Delta H = 31.6$ K.

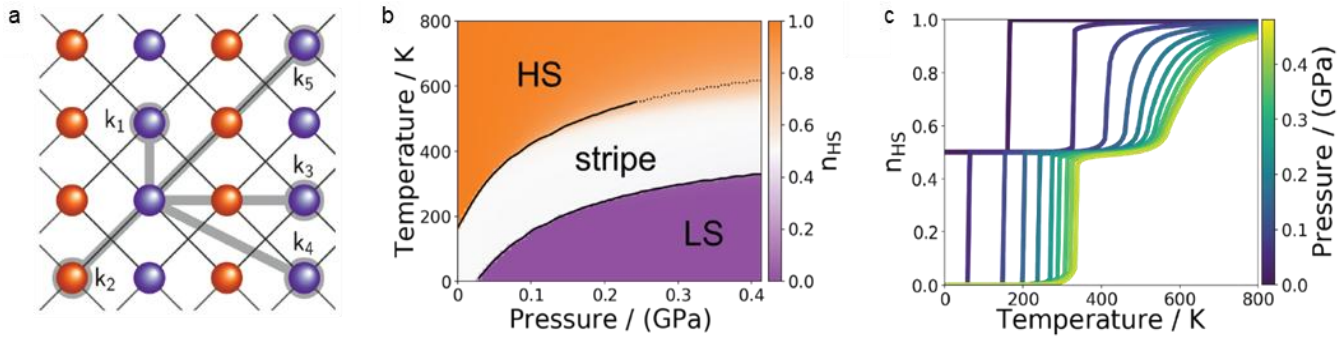

Figure 6. (a) Schematic of the 2-D Hoffmann layers showing the elastic interactions $k_1 - k_5$ and stripe order. (b) Pressure-temperature phase diagram of the elastic model (Eq. 1) on varying temperature and pressure with $k_3 = k_1/2$ and $\Delta H/k_2\delta^2 = 44\,k_1/k_2 + 43$ and fixed $k_2 = -0.911k_1$ the (through bond) second nearest neighbor interaction and δ half the difference in distance between neighboring Fe^{II} metal ions. (c) selected slices of (b).

DISCUSSION

The sensitivity of **A**·3H$_2$O to structural and spin-state perturbation via guest modification, light-irradiation and external pressure application provides a unique platform to assess elastic interaction characteristics across each of these stimuli. We have combined this with an elastic model to enable a complete overview of the structural drivers for this diverse set of SCO properties.

The framework structure of **A**·3H$_2$O shows intrinsic distortion away from a regular Hofmann architecture (i.e., multiple Fe^{II} sites & undulating layers) as driven by the disposition of the 1,2,4-triazole group to provide an array of host-host and host-guest interaction sites. This characteristic is enabled and stabilized by interaction competition, as has now been clearly established across this growing family.[8a,9] Here, the layer undulation sees two distinct interlayer environments between pairs of ligands: one contains closely aligned ligands with host-host interactions and the other shows a greater spacing between ligands and houses guest molecules with host-guest interactions. This has a flow-on effect to the SCO properties, where the crystallographically distinct Fe^{II} sites show subtle distinction in their local environments. In **A**·3H$_2$O, Fe2 shows a HS to LS transition with cooling. In the [HS-HS] state, Fe2 shows a substantially higher degree of octahedral distortion than Fe1 (Table S2), so one would expect it to remain locked into the HS state (*i.e.*, HS stabilized). This is opposite to what occurs, but, notably, is in line with that of related 2-D Hofmann systems such as [Fe(bztrz)$_2$(Pd(CN)$_2$)]·H$_2$O,EtOH (bztrz = (E)-1-phenyl-N-(1,2,4-triazol-4-yl)-methanimine))[8a] and [Fe(thtrz)$_2$Pd(CN)$_4$]·EtOH,H$_2$O (thtrz = (E)-2-(((4H-1,2,4-triazol-4-yl)imino)methyl)phenol)).[9a] This fact alone indicates that there is greater complexity to spin-state stabilization than inner coordination sphere contributions, in particular in the case of extended networks such as these, where the overall connectivity and flexibility of the framework also impact the spin-state propagation and characteristics of the through-bond and through-space elastic interactions. Highlighting the importance of framework connectivity on the properties of **A**·3H$_2$O, beyond the SCO properties arising merely from the independent transition of symmetry-inequivalent Fe^{II} sites, the interaction character between the Fe1 and Fe2 sites can be characterised as antiferroelastic, as a substantial increase in distortion occurs at Fe1 when Fe2 converts to the LS state.[6,9b,9f]

Because of the framework connectivity and the subtle balance between interactions and local Fe^{II} environments, a substantial variation to the SCO properties is realised by seemingly minor guest variation in the conversion from **A**·3H$_2$O to **A**·2H$_2$O. Magnetic susceptibility shows an upshift in the transition temperature of the [HS-HS] to [HS-LS] step, alongside the emergence of a [HS-LS] to [LS-LS] step. Structural comparison between **A**·3H$_2$O to **A**·2H$_2$O when in the [HS-HS] state reveals that partial guest removal induces a subtle decrease in the degree of octahedral distortion about Fe2; Fe1 is not significantly impacted (Table S2). This, combined with the transition temperature increase, indicates that partial guest removal acts primarily to perturb the effective ligand field strength at the Fe2 site (via steric or electronic effects, or a combination). Henceforth a low temperature [HS-LS] to [LS-LS] step in **A**·2H$_2$O is unblocked. Notably, for **A**·2H$_2$O, with SCO at Fe2 the increase in Σ for Fe1 is similar to that of **A**·3H$_2$O, suggesting that despite the upshift in transition temperature the antiferroelastic character is of a broadly similar magnitude. These findings are in line with those reported for the framework [Fe(bztrz)$_2$(Pd(CN)$_2$)]·H$_2$O,EtOH.[8a]

The elastic model supports the above findings and suggests a simple physical interpretation of guest versus SCO properties. Firstly, we find that adding more guests decreases ΔH; that is, the guests stabilize the HS state relative to the LS state. Secondly, we find that the through-bond interactions (k_2) increase as more guests are added (Figure 5(b-d)). Finally, we find that the through-space interactions (k_1 and k_5) are weak and negative in **A**·Ø and grow more negative as water is progressively added in **A**·2H$_2$O and then **A**·3H$_2$O. We note that negative spring constants correspond to the framework pushing out along that direction. This leads to the intuitively appealing picture that the guest molecules add an effective repulsive interaction (i.e., tend to push the metals apart) in the through-space directions.

It is interesting to compare these effects of guest loading versus SCO to those of hydrostatic pressure on the fully guest-loaded phase, **A**·3H$_2$O. The elastic models shows that the primary effect of pressure is to increase the effective ΔH, that is, to stabilize the LS state relative to the HS state. This demonstrates that under hydrostatic pressure, the guests introduce a negative chemical pressure on the framework. However, importantly, we also find that hydrostatic pressure does not change the elastic interactions, consistent with the previous results of Li *et al.*.[16] Therefore, unlike guest loading effects, there are no equivalents of through-bond and through-space

interaction changes with increasing hydrostatic pressure. These findings align well with structural studies which show that the [LS-LS] **A**·3H_2O framework produced under hydrostatic pressure was very different to that of the [LS-LS] framework obtained by cooling **A**·2H_2O or by the reverse-LIESST effect on **A**·3H_2O. We note that the latter two frameworks are similar in the [LS-LS] state, indicating that the subtleties of elastic interaction balance may be equally affected by partial desolvation or photo-irradiation; further elastic models would need to be developed on the LIESST and reverse-LIESST effect to confirm this.

CONCLUSIONS

By a combination of detailed experimental and theoretical modelling this study has provided a comprehensive insight into the structural and magnetic consequence of SCO induced by (1) guest modification, (2) temperature variation, (3) photoirradiation and (4) hydrostatic pressure application. In a further point of novelty, the use of this well-established 2-D Hofmann framework type has allowed a unique exploration into the structural complexities of multistep SCO under this wide range of external perturbations. Our combined structural studies and elastic models suggests a simple interpretation for the effect of the guest on the SCO properties of the host. Specifically, we find that the through-bond interactions are most affected by the inclusion of a greater number of guest molecules in the pores, whereas the through-space interactions are only weakly impacted. Therefore, simply put, the guest molecules add an effective repulsive interaction between metal ions in the through-space directions. Furthermore, the net effect of added guests on the volume of the framework depends sensitively on the detail of the cancellation of through-bond and through-space effects. Therefore, collectively, this demonstrates that while guest molecules do cause a negative chemical pressure, they also have consequences beyond the simple chemical pressure picture typically proposed.

Our detailed structural, magnetic, and elastic model results with application of variable hydrostatic pressure have revealed an important mechanistic distinction compared to guest loading. We find that while LS stabilisation occurs with greater hydrostatic pressure (as expected), increasing pressure does not significantly impact the elastic interactions.

More comprehensive structure studies of the LIESST and reverse-LIESST structures and an elastic model of LIESST and reverse-LIESST properties are required to form clear picture of the mechanism of achieving the LS state under light irradiation. Together, this will provide an important, complete picture of the structure and elastic interaction implications for SCO under this uniquely diverse set of external perturbations. Collectively, this diverse combination of structural, magnetic, and theoretical studies over this broad array of external perturbation methods (conducted on the one material) is a step towards achieving tunability and widespread applicability of these functional switchable materials.

ASSOCIATED CONTENT

Supporting Information

The Supporting Information is available free of charge at

Details on characterization, single crystal, powder diffraction, magnetic measurements, and elastic model.

Accession Codes

CCDC 2129325-2129335 contain the supplementary crystallographic data for this paper. These can be obtained free of charge via www.ccdc.cam.ac.uk/data_request/cif, or by emailing data_request@ccdc.cam.ac.uk, or by contacting The Cambridge Crystallographic Data Centre, 12 Union Road, Cambridge CB2 1EZ, UK; fax: +44 1223 336033.

AUTHOR INFORMATION

Corresponding Author

Cameron J. Kepert – *The School of Chemistry, The University of Sydney, Sydney 2006, New South Wales, Australia;* orcid.org/0000-002-6105-9706.
Email: cameron.kepert@sydney.edu.au
Benjamin J. Powell – *School of Mathematics and Physics, The University of Queensland, St Lucia, Queensland 4072, Australia.*
Email: powell@physics.uq.edu.au
Suzanne M. Neville – *The School of Chemistry, UNSW Sydney, Sydney 2052, New South Wales, Australia.* orcid.org/0000-0003-4237-4046;
Email: s.neville@unsw.edu.au

Authors

Manan Ahmed – *The School of Chemistry, UNSW Sydney, Sydney 2052, New South Wales, Australia.* orcid.org/0000-0002-7188-4152
Katrina A. Zenere – *The School of Chemistry, The University of Sydney, Sydney 2006, New South Wales, Australia;* orcid.org/0000-0003-4707-187X.
Natasha F. Sciortino – *The School of Chemistry, The University of Sydney, Sydney 2006, New South Wales, Australia;* orcid.org/0000-0003-4707-187X.
Kasun S. A. Arachchige – *School of Chemistry and Molecular Biosciences, The University of Queensland, St Lucia 4072, Queensland, Australia*; orcid.org/0000-002-7140-5596.
Gemma F. Turner – *School of Molecular Sciences, The University of Western Australia, Perth, Western Australia 6009, Australia*
Jace Cruddas – *School of Mathematics and Physics, The University of Queensland, St Lucia, Queensland 4072, Australia. Present address:* Present address: *The Institute for Photonics and Advanced Sensing, The University of Adelaide, South Australia 5005, Australia*
Carol Hua – *School of Chemistry, The University of Melbourne, Parkville, Victoria 3010, Australia. Present address: School of Life & Env Sciences, Deakin University, 3216 Victoria, Australia.*
Jason R. Price – *The Australian Synchrotron, 800 Blackburn Road, Clayton, Victoria, Australia*
Jack K. Clegg – *School of Chemistry and Molecular Biosciences, The University of Queensland, St Lucia 4072, Queensland, Australia*; orcid.org/0000-002-7140-5596.
Francisco Javier Valverde-Muñoz – *Insitut de Ciencia Molecular, Department de Quimica Inorganica, Universitat de Valéncia, Patterna, Valéncia 46980, Spain*
Jose A. Real – *Insitut de Ciencia Molecular, Department de Quimica Inorganica, Universitat de Valéncia, Patterna, Valéncia 46980, Spain*
Guillaume Chastanet – *Univ. Bordeaux, CNRS, Bordeaux-INP, ICMCB, UMR 5026, F-33600, Pessac, France*
Stephen A. Moggach – *School of Molecular Sciences, The University of Western Australia, Perth, Western Australia 6009, Australia*

ACKNOWLEDGEMENTS

We acknowledge support from Fellowships and Discovery Project funding from the Australian Research Council (ARC). Access and use of the facilities of the Australian Synchrotron was supported

by ANSTO. JKC acknowledges the support of the ARC through LE170100144. JAR thanks the Spanish Ministerio de Ciencia e Innovación (Grant PID2019-106147GB-I00; MCIN/AEI/10.13039/501100011033) and Unidad de Excelencia María de Maeztu (CEX2019-000919-M). KAZ and CJK acknowledge the facilities and the scientific and technical assistance of Sydney Analytical, a core research facility at The University of Sydney. GFT acknowledges the Australian Government for the provision of an RTP scholarship.

Notes

The authors declare no competing financial interest.

REFERENCES

1 (a) Kahn, O.; Kröber, J.; Jay, C., Spin transition molecular materials for displays and data recording. *Adv. Mater.* **1992**, *4*(11), 718-728; (b) Gütlich, P.; Garcia, Y.; Woike, T., Photoswitchable coordination compounds. *Coord. Chem. Rev.* **2001**, *219–221*, 839 ; (c) Létard, J.-F.; Guionneau, P. ; Goux-Capes, L., Spin Crossover in Transition Metal Compounds III. *Top. Curr. Chem.* **2004**, *233*, 221–249; (d) Senthil Kumar, K.; Ruben, M., Emerging trends in spin crossover (SCO) based functional materials and devices. *Coord. Chem. Rev.* **2017**, *346*, 176–205.

2 (a) Gütlich, P.; Gaspar, A. B.; Garcia, Y., Spin state switching in iron coordination compounds. *Beilstein J. Org. Chem*. **2013**, *9*(1), 342-391; (b) Halcrow, M. A., Spin-crossover materials: properties and applications, John Wiley & Sons, **2013**; (c) Gütlich, P.; Hauser, A.; Spiering, H., Thermal and optical switching of iron(II) complexes. *Angew. Chem., Int. Ed.* **1994**, *33*, 2024-2054; (d) Gütlich,P.; Goodwin, H. A., Spin crossover in transition metal compounds I. *Top. Curr. Chem.* 2004, **233**, 1–47.

3 (a) Real, J. A.; Gaspar, A. B.; Muñoz, M. C., Thermal, pressure and light switchable spin-crossover materials. *Dalton Trans.* **2005**, 2062–2079; (b) Martínez, V.; Castillo, Z. A.; Muñoz, M. C.; Gaspar, A. B.; Etrillard, C.; Létard, J.-F.; Terekhov, S. A.; Bukin, G. V.; Levchenko, G.; Real, J. A., Thermal-, Pressure-and Light-Induced Spin-Crossover Behaviour in the Two-Dimensional Hofmann-Like Coordination Polymer $[Fe(3\text{-}Clpy)_2Pd(CN)_4]$. *Eur. J. Inorg. Chem.* **2013**, *2013*, 813–818; (c) Chorazy, S.; Charytanowicz, T.; Pinkowicz, D.; Wang, J.; Nakabayashi, K.; Klimke, S.; Renz, F.; Ohkoshi, S.-I., Sieklucka, B., Octacyanidorhenate (V) Ion as an Efficient Linker for Hysteretic Two-Step Iron(II) Spin Crossover Switchable by Temperature, Light, and Pressure *Angew. Chem. Int. Ed.* **2020**, *59*, 15741–15749; (d) Kaushik, K.; Ghosh, S.; Kamilya, S.; Rouziéres, M.; Mehta, S.; Mondal, A., Reversible Photo-and Thermo-Induced Spin-State Switching in a Heterometallic $\{5d\text{-}3d\}W_2Fe_2$ Molecular Square Complex. *Inorg. Chem.* **2021**, *60*(10), 7545–7552.

4 Halcrow, M. A., Structure: function relationships in molecular spin-crossover complexes. *Chem. Soc. Rev.* **2011**, *40*, 4119–4142.

5 (a) Spiering, H., Elastic interaction in spin-crossover compounds. Spin Crossover in Transition Metal Compounds III. *Top. Curr. Chem.* **2004**, 171–195; (b) Nishino, M.; Boukheddaden, K.; Konishi, Y.; Miyashita, S., Simple two-dimensional model for the elastic origin of cooperativity among spin states of spin-crossover complexes. *Phys. Rev. Lett.* **2007**, *98*, 247203; (c) Nishino, M.; Boukheddaden, K.; Miyashita, S., Molecular dynamics study of thermal expansion and compression in spin-crossover solids using a microscopic model of elastic interactions. *Phys. Rev. B* **2009**, *79*, 012409; (d) Reeves, M. G.; Tailleur, E.; Wood, P. A.; Marchivie, M.; Chastanet, G.; Guionneau, P.; Parsons, S., Mapping the cooperativity pathways in spin crossover complexes. *Chem. Sci.* **2021**, *12*, 1007-1015.

6 (a) Collet, E.; Guionneau, P., Structural analysis of spin-crossover materials: From molecules to materials. *Compt. Ren. Chim.*, **2018**, 1133–1151; (b) Guionneau, P.; Marchivie, M.; Chastanet, G., Multiscale Approach of Spin Crossover Materials: A Concept Mixing Russian Dolls and Domino Effects. *Chem. Eur. J*. **2021**, *27*, 1483-1486.

7 (a) Paez-Espejo, M.; Sy, M.; Boukheddaden, K., Elastic frustration causing two-step and multistep transitions in spin-crossover solids: Emergence of complex antiferroelastic structures. *J. Am. Chem. Soc.* **2016**, *138*, 3202–3210; (b) Cruddas, J.; Powell, B. J., Spin-state ice in elastically frustrated spin-crossover materials. *J. Am. Chem. Soc.* **2019**, *141*, 19790–19799; (c) Cruddas, J.; Powell, B. J., Structure–property relationships and the mechanisms of multistep transitions in spin crossover materials and frameworks. *Inorg. Chem. Front.*, **2020**, *7*, 4424–4437.

8 (a) Murphy, M. J.; Zenere, K. A.; Ragon, F.; Southon, P. D.; Kepert, C. J.; Neville, S. M., Guest programmable multistep spin crossover in a porous 2-D Hofmann-type material. *J. Am. Chem. Soc.* **2017**, *139*(3), 1330-1335; (b) Liu, W.; Peng, Y.-Y.; Wu, S.-G.; Chen, Y.-C.; Hoque, N.; Ni, Z.-P.; Chen, X.-M.; Tong, M.-L., Guest-Switchable Multi-Step Spin Transitions in an Amine-Functionalized Metal–Organic Framework. *Angew. Chem., Int. Ed.* **2017**, *56*, 14982–14986.

9 (a) Klein, Y. M.; Sciortino, N. F.; Ragon, F.; Housecroft, C. E.; Kepert, C. J.; Neville, S. M., Spin crossover intermediate plateau stabilization in a flexible 2-D Hofmann-type coordination polymer. *Chem. Comm.* **2014**, *50*(29), 3838-3840; (b) Milin, E.; Patinec, V.; Triki, S.; Bendeif, E.-F.; Pillet, S.; Marchivie, M.; Chastanet, G.; Boukheddaden, K., Elastic frustration triggering photoinduced hidden hysteresis and multistability in a two-dimensional photoswitchable Hofmann-like spin-Crossover metal–organic framework. *Inorg. Chem.* **2016**, *55*(22), 11652–11661; (c) Sciortino, N. F.; Zenere, K. A.; Corrigan, M. E.; Halder, G. J.; Chastanet, G.; Létard, J.-F.; Kepert, C. J.; Neville, S. M., Four-step iron (II) spin state cascade driven by antagonistic solid-state interactions. *Chem. Sci.* **2017**, *8*(1), 701-707; (d) Zenere, K. A.; Duyker, S. G.; Trzop, E.; Collet, E.; Chan, B.; Doheny, P. W.; Kepert, C. J.; Neville, S. M., Increasing spin crossover cooperativity in 2D Hofmann-type materials with guest molecule removal. *Chem. Sci.* **2018**, *9*(25), 5623-5629; (e) Sciortino, N. F.; Ragon, F.; Zenere, K. A.; Southon, P. D.; Halder, G. J.; Chapman, K. W.; Pineiro-Lopez, L.; Real, J. A.; Kepert, C. J.; Neville, S. M., Exploiting pressure to induce a "guest-blocked" spin transition in a framework material. *Inorg. Chem*. **2016**, *55*(20), 10490–10498; (f) Brennan, A. T.; Zenere, K. A.; Brand, H. E.; Price, J. R.; Bhadbhade, M. M.; Turner, G. F.; Moggach, S. A.; Valverde-Muñoz, F. J.; Real, J. A.; Clegg, J. K.; Neville, S. M., Guest Removal and External Pressure Variation Induce Spin Crossover in Halogen-Functionalized 2-D Hofmann Frameworks. *Inorg. Chem.* **2020**, *59*(19), 14296–14305; (g) Ndiaye, M. M.; Pillet, S.; Bendeif, E.-E.; Marchivie, M.; Chastanet, G.; Boukheddaden, K.; Triki, S., Hidden Hysteretic Behavior of a Paramagnetic Fe (II) Network Revealed by Light Irradiation. *Eur. J. Inorg. Chem.* **2017**, *3-4*, 305–313; (h) Brennan, A. T.; Zenere, K. A.; Clegg, J. K.; Neville, S. M., Three Distinct Spin-Crossover Pathways in Halogen-Appended 2D Hofmann Frameworks. *Inorg. Chem.* **2021**, *60*(6), 3871-3878.

10 Scott, S.; Ross, T. M.; Moubaraki, B.; Murray, K. S.; Neville, S. M., Spin crossover in polymeric materials using Schiff base functionalized triazole ligands. *Eur. J. Inorg. Chem*. **2013**, *5-6*, 803–812.

11 Létard, J.-F. ; Guionneau, P. ; Rabardel, L.; Howard, J. A. K.; Goeta, A. E.; Chasseau, D. ; Kahn, O., Structural, magnetic, and photomagnetic studies of a mononuclear iron(II) derivative exhibiting an exceptionally abrupt spin transition. Light-induced thermal hysteresis phenomenon. *Inorg. Chem.* **1998**, *37*, 4432–4441.

12 (a) Hauser, A., Light-induced spin crossover and the high-spin → low-spin relaxation. Spin crossover in transition metal compounds II. *Top. Curr. Chem*. **2004**, *234*, 155–198; (b) Létard, J.-F., Photomagnetism of iron(II) spin crossover complexes-the T(LIESST) approach. *J. Mater. Chem.* **2006**, *16*, 2550–2559.

13 (a) Létard, J.-F.; Capes, L.; Chastanet, G.; Moliner, N.; Létard, S.; Real, J. A.; Kahn, O., Critical temperature of the LIESST effect in iron(II) spin crossover compounds. *Chem. Phys. Lett*. **1999**, *313*, 115–120; (b) Marcen, S.; Lecren, L.; Capes, L.; Goodwin, H. A.; Létard, J.-F., Critical temperature of the LIESST effect in a series of hydrated and anhydrous complex salts $[Fe(bpp)_2]X_2$. *Chem. Phys. Lett*. **2002**, *358*, 87–95; (c) Létard, J.-F.; Guionneau, P.; Nguyen, O.; Costa, J. S.; Marcén, S.; Chastanet, G.; Marchivie, M.; Goux-Capes, L., A guideline to the design of molecular-based materials with long-lived photomagnetic lifetimes. *Chem. Eur. J*. **2005**, *11*, 4582–4589; (d) Chastanet, G.; Desplanches, C.; Balde, C.; Rosa, P.; Marchivie, M.; Guionneau, P., A critical review of the *T*(LIESST) temperature in spin crossover materials – What it is and what it is not. *Chem. Sq.* **2018**, *2*, 2-18.

14 Guionneau, P., Crystallography and spin-crossover. A view of breathing materials. *Dalton Trans.* **2014**, *43*, 382-393.

15 (a) Chapman, K. W.; Halder, G. J.; Chupas, P. J., Guest-dependent high pressure phenomena in a nanoporous metal– organic framework material. *J. Am. Chem. Soc.* **2008**, *130*, 10524–10526; (b) Lapidus, S. H.; Halder, G. J.; Chupas, P. J.; Chapman, K. W., Exploiting high pressures to generate porosity, polymorphism, and lattice expansion in the nonporous molecular framework $Zn(CN)_2$. *J. Am. Chem. Soc*. **2013**, *135*, 7621–7628; (c) Chapman, K. W.; Halder, G. J.; Chupas, P. J., Pressure-induced amorphization and porosity modification in a metal–organic framework. *J. Am. Chem. Soc.* **2009**, *131*, 17546–17547.

16 Li, R.; Levchenko, G.; Valverde-Muñoz, F. J.; Gaspar, A. B.; Ivashko, V. V.; Liu, B.; Yuan, M.; Fylymonov, H.; Real, J. A., Pressure Tunable Electronic Bistability in Fe(II) Hofmann-like Two-Dimensional Coordination Polymer $[Fe(Fpz)_2Pt(CN)_4]$: A Comprehensive Experimental and Theoretical Study. *Inorg. Chem.* **2021**, *60*(21), 16016-16028.

For Table of Contents Only

SYNOPSIS TOC. Spin-crossover in a new 2-D Hofmann framework is induced under a diverse set of external perturbations (temperature, pressure, light-irradiation and guest exchange) - a comprehensive picture of the structure and magnetism are presented across each of these triggers.